Taguchi method modelling of Nd:YAG laser ablation of microchannels on cyclic olefin polymer film

Ronán McCann[a, b, c, d], Komal Bagga[a, b, c*], Gabriel Duaux[a,b], Apryll Stalcup[c,e], Mercedes Vázquez[a, c, e], Dermot Brabazon[a, b, c, d]

[a]Advanced Processing Technology Research Centre, Dublin City University, Glasnevin, Dublin 9, Ireland

[b]School of Mechanical and Manufacturing Engineering, Dublin City University, Glasnevin, Dublin 9, Ireland

[c]Irish Separation Science Cluster, National Centre for Sensor Research, Dublin City University, Glasnevin, Dublin 9, Ireland

[d]National Centre for Plasma Science and Technology, Dublin City University, Dublin 9, Glasnevin, Ireland

[e]School of Chemical Sciences, Dublin City University, Glasnevin, Dublin 9, Ireland

---

***Corresponding Author:**

Dr. Komal Bagga

Advanced Processing Technology Research Centre,

Dublin City University, Dublin 9, Ireland

Tel: + 353 1 700 7603

E-mail: komal.bagga@dcu.ie

Abstract

This paper presents the development of a model for Nd:YAG laser ablation of cyclic olefin polymer (COP) films. Two Taguchi orthogonal array experimental designs were implemented

to produce a model for the prediction of microchannel depth and width produced on ZeonorFilm® ZF14 and ZF16 polymer films via laser ablation. The width and depth of the produced microchannels were measured using 3D optical profilometry. Microchannels produced were seen to range in depth of up to 50 µm, and widths of 112 µm via single-pass laser depending on the grade of COP, with feature size increasing as the number of laser passes increased. The models are discussed in terms of adjusted coefficient of determination, signal to noise ratio and model significance. The effect of the process parameters used such as fluence and scan speed on three different grades of COP was examined with an aim to produce a simple model suitable for predictive control of surface microstructuring of COP.

Keywords: Laser ablation; cyclic olefin polymer; microchannel fabrication; Nd:YAG; picosecond; ZeonorFilm®

1. Introduction

Cyclic olefin polymer (COP) and cyclic olefin copolymer (COC) are increasingly popular substrate materials replacing traditional polymers such as polymethyl methacrylate (PMMA), polycarbonate (PC) and polydimethylsiloxane (PDMS) in analytical applications [1]. COC and COP have been reported for use in a wide variety of applications ranging from diffractive optic elements [2], waveguide coatings [3] and as substrates for the deposition of nanomaterial films [4] which exploit the polymer's high transparency in the UV-Visible-NIR range. Furthermore, COPs and COCs have also been exhibits excellent biocompatibility which allows them to find application in high-adhesion biomimetic surfaces [5] and cell culturing platforms [6]. As COP and COC are also noted for low water absorption and resistance to acids, bases and most non-hydrocarbon solvents, they offer an excellent alternative for liquid analysis platforms which have been typically fabricated using PDMS and PMMA to-date.

With increasing applications, the need to develop new processing techniques for the manufacture of devices utilising COP and COC becomes critically important. Techniques such as injection moulding [7], embossing [8], xurography [9], 3D-printing [10] and micromilling [11] have all been successful in the creation of micro- and nanoscale features on COC and COP substrates. Laser processing offers the ability for rapid, single-step prototyping of devices. To-date, laser processing of COC and COP has been examined using excimer [12,13], femtosecond titanium sapphire [14] and carbon dioxide lasers [15,16]. Recently, the use of solid-state neodymium-doped aluminium garnet (Nd:YAG) lasers has also been examined for microchannel fabrication on COP [17].

In this paper, we present an investigation into laser ablation of ZeonorFilm® ZF14 and ZF16 COP using an industrial picosecond pulsed neodymium-doped yttrium aluminium garnet (Nd:YAG) laser. The effect of parameters such as laser fluence, beam scan speed and number of passes on the depth and width of the produced microchannels was examined. A Taguchi orthogonal Design of Experiments (DoE) was then used to develop a model for the ablation of two grades and three thicknesses of COP with an aim to develop a simple protocol suitable for model predictive control of machining of COP.

2. Methods and Materials

2.1 Experimental Setup

The experimental setup is shown in

Figure 1. The laser used was a WEDGE HF 1064 (BrightSolutions, Italy) 1064 nm diode-pumped solid-state Nd:YAG. The laser had a pulse width of 700 ps, a pulse repetition frequency of 10 kHz, a maximum average power output of 4 W and a maximum pulse energy of 160 µJ. The beam was rastered in the xy-plane unidirectionally using an SS-12 2D-scanning galvanometer (Raylase, Germany) to form microchannels separated by 200 µm. The sample

was positioned in the laser beam waist using a 404-4PD single-axis nanoposition stage (PI, Germany) at a laser spot size of 140 µm.

Microchannel morphology was examined using a VHX-2000 3-dimensional optical profilometer (Keyence, Japan) scanning upwards from the base of the channel in 1 µm increments. The average measurement of 16 channel profiles (four profiles across four channels) per sample at a 500x magnification were recorded where the channels were examined for two parameters: depth (defined as the length from the base of the channel to the mean height of the channel crests) and full-width half-max (FWHM, defined as the width of the channel measured at half the depth of the channel).

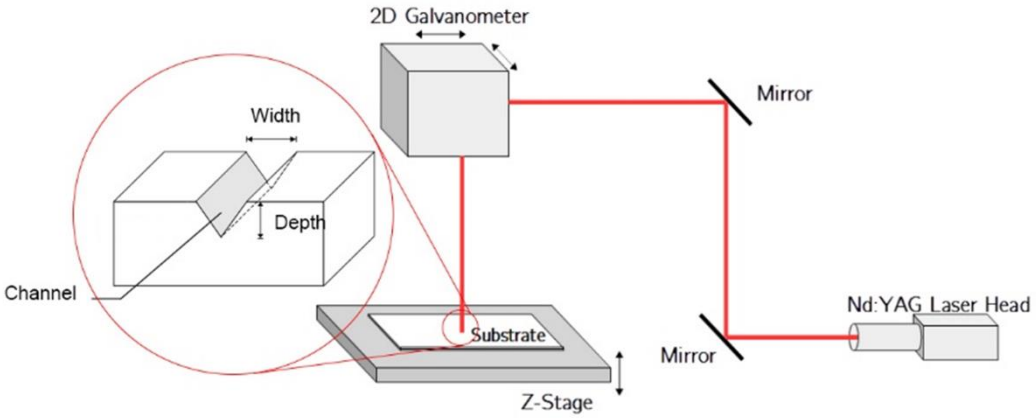

Figure 1: Schematic of the 1064 nm laser ablation setup and responses measured.

2.2 Materials

The substrates used in this experiment were ZeonorFilm® ZF14-188, ZF16-100 and ZF16-250 cyclic olefin polymer (Zeon Chemical LP, Japan) with film thicknesses of 188 µm, 100 µm and 250 µm respectively. Material properties of note are listed in Table 1.

Table 1: Material properties of ZeonorFilm® ZF14 and ZF16 grades of cyclic olefin polymer [17,18].

Property	ZF14	ZF16
Water Absorbency (%)	<0.01	
Glass Transition Temperature (°C)	136	163
Refractive Index	1.53	
Birefringence (nm)	3	
Effective optical penetration depth at 1064 nm (nm)	140	

2.3 Taguchi Orthogonal Array

The experimental design chosen for the study of laser ablation of ZF14 was a Taguchi orthogonal array L_{16} (with three factors at four levels, outlined in Table 2) and was produced and analysed using the Design-Expert 7 (Stat-Ease Inc., USA) and Minitab 17 (Minitab Inc., USA) software packages. The minimum fluence level of the design was chosen to be above the threshold fluence for ablation. Previous work by our group determined a threshold fluence for ZF14-188 of 0.32 J/cm^2 for a single laser pass and a beam scan speed of 1.2 mm/s [17]. A reduced quadratic model was developed using a backwards elimination to remove insignificant terms and increase model simplicity while maximising the adjusted coefficient of determination.

Table 2: Process parameters and design levels used. The thickness parameter was excluded from the ZF14 model.

Factors	Symbol	Unit	Level 1	Level 2	Level 3	Level 4
Fluence	F	J.cm^{-2}	0.652	0.785	0.896	0.983
Scan Speed	v	mm.s^{-1}	1.8	2.5	3	3.5
Number of passes	N	unitless	1	2	3	4
Thickness	d	µm	100	250	-	-

Similarly, for the ZF16 ablation study, an L_{32} matrix ($2^1 + 4^9$) was used by coupling two L_{16} matrices using the same levels as before with a fourth factor, film thickness, added to the experimental design with two levels. A reduced quadratic model was developed for the ZF16 ablations with a backwards elimination applied as before. The full orthogonal arrays for the ZF14 and ZF16 models are listed in Tables 1S and 2S respectively in the ESI.

3. Results and Discussion

3.1 Microchannel Morphology

Figure 2 shows the typical microchannel morphologies produced via laser ablation as measured via 3D optical profimometry. Across all samples, the microchannels produced had a v-shaped morphology, which is consistent with previous work on infrared laser ablation of COP with deeper microchannels having a more pronounced V-shape. Along the base of the microchannels were isolated wells, which became less pronounced as the microchannels became deeper. This was attributed to the pulsed nature of the applied scanning beam of radiation. Outside the ablation site, condensed melt and debris was seen, again being more evident with deeper channels. For deeper microchannels, the debris was seen to be more smoother, suggesting that melting occurred m

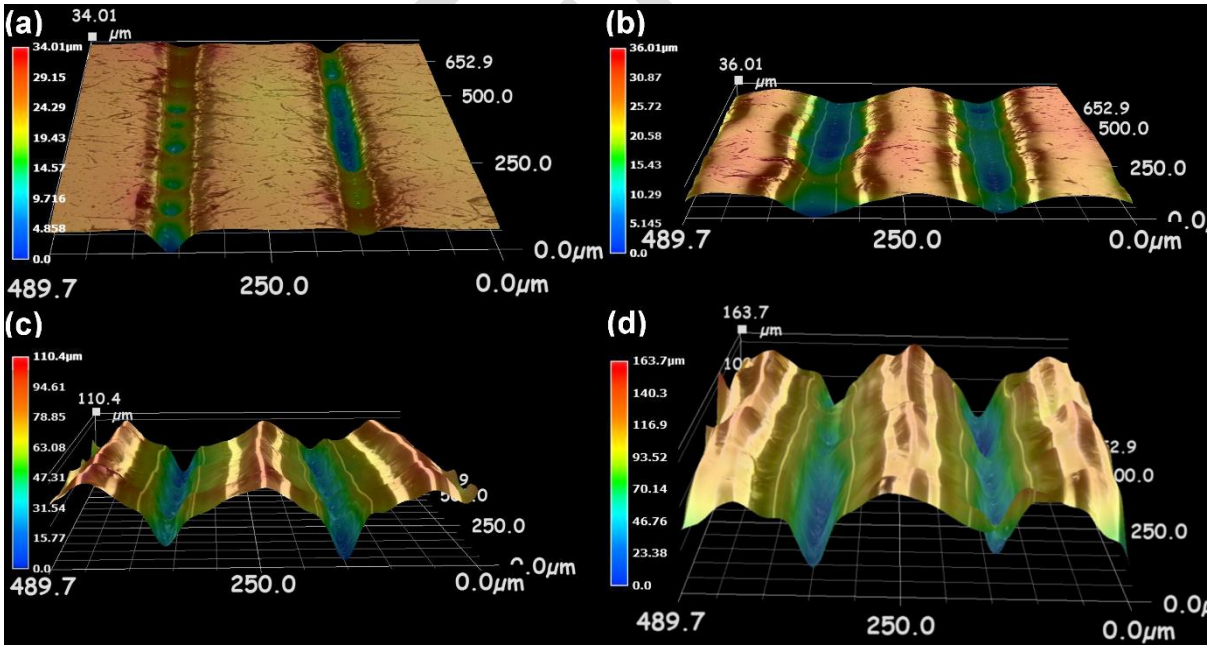

Figure 2: 3D Optical Profilometry images showing the formation of (a) 6 µm, (b) 25 µm and (c) 87 µm microchannels on ZF14-188 and (d) a 83 µm microchannel on ZF16-250.

3.2 Signal-to-Noise Analysis

To determine which factors had the greatest effect in the model, the signal-to-noise (S/N) ratio was calculated for the depth and FWHM profilometry measurements. Many analytical devices require microchannels with high surface area-to-volume ratios, for enhanced surface-chemical interaction or increased mass transfer for example [19,20]. As analytical applications are of particular interest in this study, a target for high aspect ratio channels (i.e. large depth and small width) was decided. Two different S/N ratios were decided upon based on these experimental goals. Equations 1 and 2 show the S/N ratio definitions used for the FWHM and depth respectively.

$$\frac{S}{N}(\text{FWHM}) = -10\, log_{10}\left(\sum \frac{y^2}{n}\right) \quad (1)$$

$$\frac{S}{N}(\text{Depth}) = -10\, log_{10}\left(\sum \frac{y^{-2}}{n}\right) \quad (2)$$

Table 3 outlines the calculated S/N ratios for the ZF14 experimental design. Fluence showed the largest delta (i.e. the difference between the maximum and minimum recorded response values) for both depth and FWHM.

Table 3: Responses for the signal-to-noise ratio of microchannel depth and FWHM measurements for ZF14.

Response	Factor	Level 1	2	3	4	Delta	Rank
Depth	F	12.42	21.87	29.68	29.84	17.42	1
	ν	27.92	23.20	21.67	21.01	6.91	2
	N	21.31	21.80	25.63	25.06	4.32	3
FWHM	F	-29.80	-34.49	-36.85	-35.28	7.05	1
	ν	-33.63	-33.77	-34.17	-34.84	1.21	2
	N	-33.70	-34.12	-34.05	-34.56	0.86	3

The additional design factor, film thickness, used in the ZF16 experimental design was found to be the second ranked factor (in terms of delta) affecting the produced microchannel depth (Table 4). The effect of substrate thickness was however the lowest ranked factor affecting the FWHM response, suggesting it has the smallest effect of all experimental factors

on the FWHM over the range studied. The S/N ratios for the experimental factors of the ZF14 and ZF16 are also shown in Figures 1S and 2S respectively in the ESI.

Table 4: Responses for the signal-to-noise ratio of microchannel depth and FWHM measurements for ZF16.

Response	Factor	Level 1	2	3	4	Delta	Rank
Depth	F	16.10	21.58	28.80	33.26	17.16	1
	ν	26.87	24.33	24.23	24.31	2.63	3
	N	24.44	24.49	25.85	24.96	1.41	4
	d	28.14	21.73	-	-	6.41	2
FWHM	F	-28.58	-30.77	-35.63	-37.63	9.05	1
	ν	-33.22	-32.50	-33.45	-33.44	0.95	3
	N	-32.31	-32.91	-33.90	-33.49	1.59	2
	d	-33.62	-32.69	-	-	0.93	4

3.3 ANOVA Analysis

Table 5 outlines the primary Analysis of Variance (ANOVA) parameters extracted from the depth and FWHM models. All models developed had an adjusted R-squared of greater than 0.83, and were all in close agreement (within 0.1) with the model predicted R-squared. The adequate precision (i.e. the signal-to-noise ratio) of the 4 responses was large, indicating that error is not a significant contribution to the model. The F-value, which compares the parameter variance with the residual variance, was also large for all models again indicating strong model significance. Full ANOVA information for both models is listed in Tables 3S – 6S in the ESI.

Table 5. Primary ANOVA parameters for the four Taguchi models.

Response	Material	Degrees of Freedom	Adjusted R-Squared	Predicted R-Squared	Adequate Precision	F value
FWHM	ZF14	6	0.985	0.973	34.276	167.32
	ZF16	7	0.854	0.811	15.7	26.94
Depth	ZF14	4	0.947	0.911	25.1	67.35
	ZF16	7	0.828	0.770	16.3	22.25

The equations derived from the Taguchi model were:

$$z_{\mathrm{ZF14}} = (2.81 - 6.01F + 0.23N - 0.28FN + 3.54F^2)^{-2} \quad (3)$$

$$z_{\mathrm{ZF16}} = exp(1.60 - 0.01t + 1.05F + 0.44\nu - 0.70N + 0.02dF - 2.58 \times 10^{-3}t\nu + 0.89FN) \quad (4)$$

$$w_{ZF14} = (0.05 - 0.12F + 4.70 \times 10^{-3}\nu - 3.61 \times 10^{-4}N - 3.88 \times 10^{-3}F\nu + 0.07F^2 - 3.42 \times 10^{-4}\nu^2)^{0.68} \quad (5)$$

$$w_{ZF16} = (0.05 - 1.60 \times 10^{-4}\mathrm{d} - 0.02F + 0.04\nu - 0.01N + 2.01 \times 10^{-4}dF - 0.04F\nu + 0.01FN)^{-1} \quad (6)$$

where z is microchannel depth (in µm), w is microchannel FWHM (in µm), F is laser fluence (in J/cm^2), N is number of laser passes and ν is laser beam scan speed (in mm/s). The simplest model derived was for ZF-14 microchannel depth, with only 4 significant factors, and 4 degrees of freedom in the model (Equation 3). For ZF16 microchannel depth, the model was more complex with 4 factors and 7 degrees of freedom, and an exponential transformation applied, shown in Equation 4. This exponential behaviour of the model, coupled with fluence having the largest effect of all the process parameters, is an expected behaviour resulting from the *Beer-Lambert Law* whereby light absorption is exponential to the applied radiation intensity [17]. The microchannel FWHM models for ZF14 and ZF16 had 6 and 7 degrees of freedom, and 3 and 4 factors respectively (shown in Equations 5 and 6).

Non-linear factors in model equations, such as the F^2 term in Equation 3, are a measure of the saturation of the response as the factor increases [21]. From Equation 3, it was determined that 0.88 J/cm^2 was the optimal fluence for processing of ZF14 grade COP, with a reduction in the measured depth response for fluences greater than 0.88 J/cm^2. Similarly, two non-linear factors, scan speed and fluence, were evident in the model for microchannel width on ZF14, as shown in Equation 5.

No other factors effecting the saturation of microchannel depth or width was evident for either the ZF14 or ZF16 grade polymers. This is due to limitations in the Taguchi method being optimised to accurately map the process space in a minimal number of experimental runs. As such, this limitation makes it difficult to extrapolate beyond the process space. It is possible that if the process space is extended beyond the maximum level chosen in this study, the saturation in microchannel depth will become evident for ablations on ZF16.

3.4 Microchannel Depth

The ZF14-188 model predicted a maximum microchannel depth of 23 µm (Figure 3a), while depths of 50 µm and 36 µm (Figures 4a and 5a) were predicted for the ZF16-100 and ZF16-250 respectively. The non-linearity of the depth response to fluence is consistent to that previously reported for 1064 nm laser ablation of ZF14-188, which was attributed to plume occlusion, whereby the ablation plume becomes opaque at the laser wavelength thus reducing fluence at the ablation site [17]. Ablation on the ZF16 polymers revealed a positive linear correlation between both fluence and number of passes, and microchannel depth over the range modelled. This was attributed both to ZF16 having a higher glass transition temperature (T_g) than ZF14 [18] and the differing substrate thicknesses. A higher T_g would limit the thermal effects and would result in a larger heat affected zone during laser processing. This larger heat affected zone would resulting in less melt and macro-particulates ejected from the ablation site during processing, thus mitigating occlusion of the substrate surface by the ablation plume during processing. The difference between the maximum predicted depth of channels on the ZF16-100 and ZF16-250 was again attributed to the thicker substrate having a larger thermal mass, thereby resulting in less heat accumulation and thus a lower working temperature during laser processing. This lower working temperature would limit the "incubation effect" whereby changes to the mechanical or chemical properties can occur during multi-shot laser ablation [22]. This incubation effect can lead to lower ablation threshold values as a function of number of laser shots as the substrate builds up heat during processing. The linearity of the depth response with both fluence, beam scan speed and number of passes suggests that plume occlusion is not a significant effect for ZF16 within the examined process space.

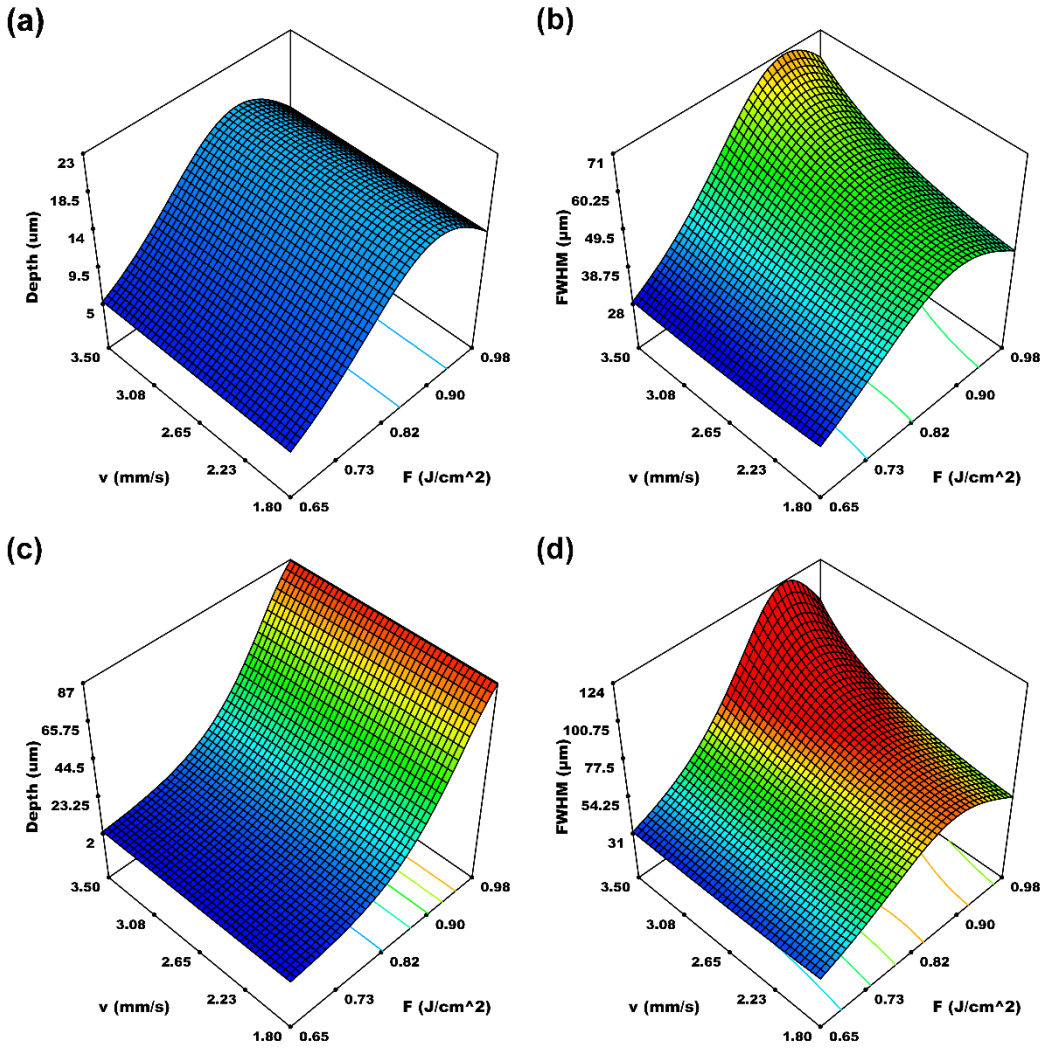

202

203 Figure 3: Surface plots of the effect of fluence and scan speed on the microchannel depth and FWHM responses on
204 ZF14-188 for one laser pass (a-b) and four laser passes (c-d).

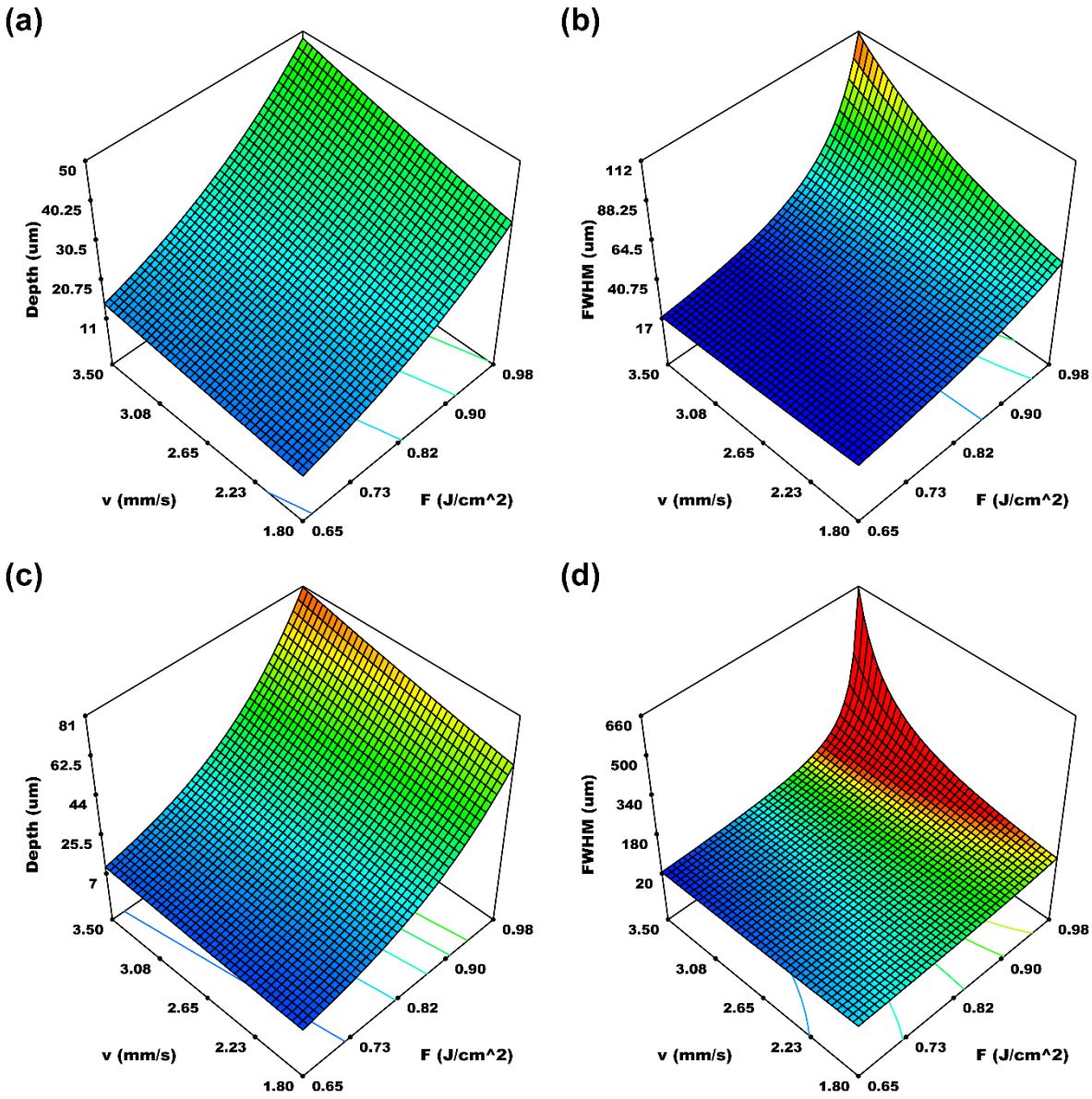

205

206 Figure 4: Surface plots of the effect of fluence and scan speed on the microchannel depth and FWHM responses on
207 ZF16-100 for one laser pass (a-b) and four laser passes (c-d).

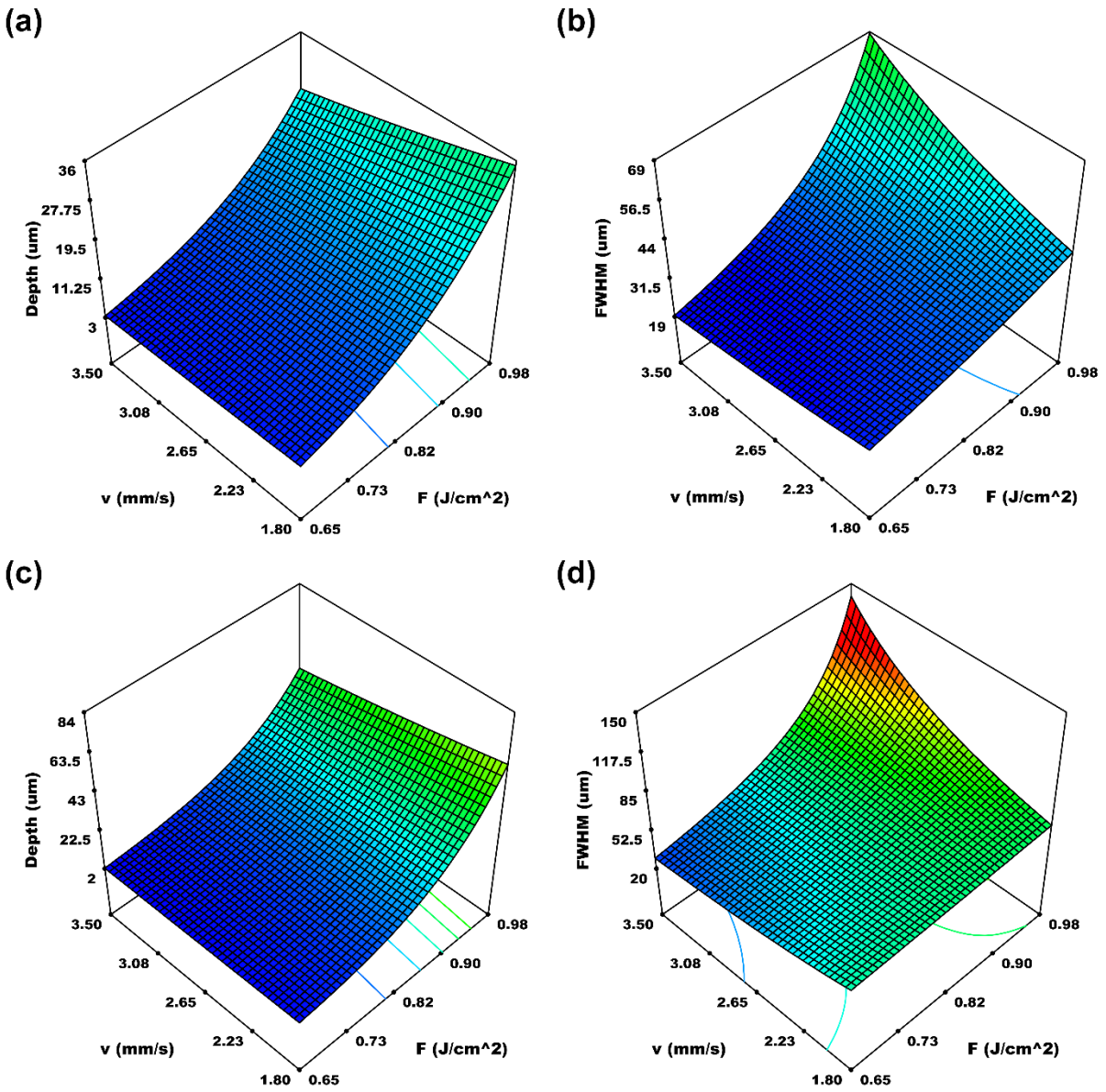

Figure 5: Surface plots of the effect of fluence and scan speed on the microchannel depth and FWHM responses on ZF16-250 for one laser pass (a-b) and four laser passes (c-d).

For four laser passes (the maximum trialled), increased microchannel depths were evident on all substrates. Maximum depths of up to 87 µm were predicted via the Taguchi model for ZF14 (Figure 3c). For ZF16-100 and ZF16-250, depths of 81 µm and 58 µm were found respectively (Figures 4c and 5c), similar to the ZF14 model. Smaller minima were predicted for the microchannel depths for multiple pass ablations when compared to the single

pass, which may be indicative of decreasing model significance at the edge of the process space.

3.5 Microchannel Full-Width Half-Maximum

For single pass laser ablation of ZF14-188, the model predicted maximum channel widths of 71 µm was found (Figure 3b). At both high and low scan speeds, the FWHM was seen not to scale linearly with fluence. This non-linearity is consistent with previous work which showed a logarithmic increase of microchannel width, though with decreasing reproducibility [17]. The model predicted microchannel width was also seen to be highly dependent on scan speed, with higher scan speeds resulting in wider channels. This suggested that plume occlusion was also an important mechanism at slower scan speeds, with the plume opacity inversely proportional to scan speed.

The ZF16 model predicted a maximum of 112 µm and 69 µm for ZF16-100 and ZF16-250 respectively, as shown in Figure 4b and 5b respectively. This discrepancy was attributed to the thicker substrate having a larger thermal mass, thus maintaining a lower working temperature and thus a lower ablation threshold during processing.

Maximum microchannel widths of 124 µm were seen for four laser passes on ZF14 (Figure 3d), which was higher than that previously reported for 1064 nm laser ablation of ZF14 [17]. Though the process conditions differed slightly in the two studies, the non-linear relationship, again most likely due to plume occlusion, between number of laser passes, scan speed and fluence suggested an optimal processing condition was possible for maximising microchannel width. The ZF16 model showed a maximum of 660 µm and 180 µm respectively for ZF16-100 and ZF16-250 widths (Figures 4d and 5d). Previous studies on 1064 nm laser ablation of ZF14 have seen melting and warping of the substrate for high numbers of passes, whereby the substrate may similarly be experiencing a build-up in heat during processing [17].

The large maximum value modelled on ZF16-100 suggested that the model was at the edge of the usable process space for the material prior to melting or warping occurring.

4. Conclusions

In conclusion, this paper presents the first developed model for the laser ablation of two different grades of ZeonorFilm® COP. It was demonstrated that using an industrial Nd:YAG laser, it is possible to finely control the machining of microchannels on the surface of COP, with differing responses for different grades of COP. The primary factor effecting the microchannel depth and FWHM on both ZF14 and ZF16 was the laser fluence, however the model developed for laser structuring of ZF16 showed that the number of laser passes and substrate thickness were also significant factors effecting the depth and FWHM responses. For ablation of ZF14, a maximum fluence of 0.88 J/cm^2 was found to be optimal. The differing glass transition temperatures of the two grades of COP were seen to drive the difference in the predicted responses of structures on ZF14 and ZF16. When comparing two thickness of the ZF16 polymer, the thermal bulk of the two thicknesses was attributed to be a primary reason for different responses of the two materials. This differing thermal bulk would result in different rates in heat accumulation and the working temperature during processing. Some limitations of the Taguchi model were seen when examining the edge of, and when extrapolating beyond, the process space. Ultimately, the developed model presented allows for the implementation of predictive control of surface structuring of ZeonorFilm® COP via laser ablation over the process space examined.

Acknowledgements

This publication has emanated from research conducted with the financial support of Science Foundation Ireland (SFI) under Grant Number 12/IA/1576, the European Union's Horizon 2020 Research and Innovation Program under the Marie Sklodowska-Curie grant agreement

No. 655194. R. McCann would like to thank Mr. Ben Delaney of the Dublin City University School of Physical Sciences for the many productive discussions during this work.

References

[1] P.S. Nunes, P.D. Ohlsson, O. Ordeig, J.P. Kutter, Cyclic olefin polymers: Emerging materials for lab-on-a-chip applications, Microfluid. Nanofluidics. 9 (2010) 145–161. doi:10.1007/s10404-010-0605-4.

[2] A.-K. Holthusen, O. Riemer, J. Schmütz, A. Meier, Mold machining and injection molding of diffractive microstructures, J. Manuf. Process. 26 (2017) 290–294. doi:10.1016/j.jmapro.2017.02.014.

[3] Y.-W. Shi, Y. Wang, Y. Abe, Y. Matsuura, M. Miyagi, S. Sato, M. Taniwaki, H. Uyama, Cyclic olefin polymer-coated silver hollow glass waveguides for the infrared, Appl. Opt. 37 (1998) 7758. doi:10.1364/AO.37.007758.

[4] S. Inguva, R.K. Vijayaraghavan, E. McGlynn, J.-P. Mosnier, Highly transparent and reproducible nanocrystalline ZnO and AZO thin films grown by room temperature pulsed-laser deposition on flexible Zeonor plastic substrates, Mater. Res. Express. 2 (2015) 96401. doi:10.1088/2053-1591/2/9/096401.

[5] H. Liu, J. Choi, G. Zaghi, J. Zhang, C. Carraro, R. Maboudian, Frictional characteristics of stiff, high aspect ratio microfiber arrays based on cyclic olefin polymers, J. Adhes. Sci. Technol. 31 (2017) 1017–1027. doi:10.1080/01694243.2016.1240024.

[6] K. Bagga, R. McCann, F. O'Sullivan, P. Ghosh, S. Krishnamurthy, A. Stalcup, M. Vázquez, D. Brabazon, Nanoparticle functionalized laser patterned substrate: an innovative route towards low cost biomimetic platforms, RSC Adv. 7 (2017) 8060–8069. doi:10.1039/C6RA27260F.

[7] H.-L. Lin, C.-S. Chen, R.-T. Lee, S.-C. Chen, R.-D. Chien, M.-C. Jeng, J.-R. Hwang, Effects of Process Parameters on Replication Accuracy of Microinjection Molded Cyclic Olefins Copolymers Parts, Jpn. J. Appl. Phys. 52 (2013) 44001. doi:10.7567/JJAP.52.044001.

[8] K. Metwally, L. Robert, S. Queste, B. Gauthier-Manuel, C. Khan-Malek, Roll manufacturing of flexible microfluidic devices in thin PMMA and COC foils by embossing and lamination, Microsyst. Technol. 18 (2012) 199–207. doi:10.1007/s00542-011-1358-z.

[9] A. Ben Azouz, S. Murphy, S. Karazi, M. Vázquez, D. Brabazon, Fast Fabrication Process of Microfluidic Devices Based on Cyclic Olefin Copolymer, Mater. Manuf. Process. 29 (2014) 93–99. doi:10.1080/10426914.2013.811739.

[10] N. Bhattacharjee, A. Urrios, S. Kang, A. Folch, The upcoming 3D-printing revolution in microfluidics, Lab Chip. 16 (2016) 1720–1742. doi:10.1039/C6LC00163G.

[11] J. Steigert, S. Haeberle, T. Brenner, C. Müller, C.P. Steinert, P. Koltay, N. Gottschlich, H. Reinecke, J. Rühe, R. Zengerle, J. Ducrée, Rapid prototyping of microfluidic chips in COC, J. Micromechanics Microengineering. 17 (2007) 333–341. doi:10.1088/0960-1317/17/2/020.

[12] D. Sabbert, J. Landsiedel, H.-D. Bauer, W. Ehrfeld, ArF-excimer laser ablation experiments on Cycloolefin Copolymer (COC), Appl. Surf. Sci. 150 (1999) 185–189. doi:10.1016/S0169-4332(98)00334-1.

[13] P.W. Leech, Effect of norbornene content on laser ablation of cyclic olefin copolymers, Mater. Des. 31 (2010) 4858–4861. doi:10.1016/j.matdes.2010.05.038.

[14] R. Suriano, A. Kuznetsov, S.M. Eaton, R. Kiyan, G. Cerullo, R. Osellame, B.N. Chichkov, M. Levi, S. Turri, Femtosecond laser ablation of polymeric substrates for the fabrication of microfluidic channels, Appl. Surf. Sci. 257 (2011) 6243–6250. doi:10.1016/j.apsusc.2011.02.053.

[15] J. Cai, J. Jiang, F. Gao, G. Jia, J. Zhuang, G. Tang, Y. Fan, Rapid prototyping of cyclic olefin copolymer based microfluidic system with CO2 laser ablation, Microsyst. Technol. (2017) 1–7. doi:10.1007/s00542-017-3282-3.

[16] F. Bundgaard, G. Perozziello, O. Geschke, Rapid prototyping tools and methods for all-Topas® cyclic olefin copolymer fluidic microsystems, Proc. Inst. Mech. Eng. Part C J. Mech. Eng. Sci. 220 (2006) 1625–1632. doi:10.1243/09544062JMES295.

[17] R. McCann, K. Bagga, R. Groarke, A. Stalcup, M. Vázquez, D. Brabazon, Microchannel fabrication on cyclic olefin polymer substrates via 1064 nm Nd:YAG laser ablation, Appl. Surf. Sci. 387 (2016) 603–608. doi:10.1016/j.apsusc.2016.06.059.

[18] ZeonorFilm® isotropic optical film properties [Internet]. Zeon Corporation, (2017) Available from: http://www.zeon.co.jp (accessed June 1, 2017).

[19] J. Hansson, H. Yasuga, T. Haraldsson, W. van der Wijngaart, Synthetic microfluidic paper: high surface area and high porosity polymer micropillar arrays, Lab Chip. 16 (2016) 298–304. doi:10.1039/C5LC01318F.

[20] Z. Dong, C. Yao, Y. Zhang, G. Chen, Q. Yuan, J. Xu, Hydrodynamics and mass transfer of oscillating gas-liquid flow in ultrasonic microreactors, AIChE J. 62 (2016) 1294–

1307. doi:10.1002/aic.15091.

[21] G. Savriama, F. Baillet, L. Barreau, C. Boulmer-Leborgne, N. Semmar, Optimization of diode pumped solid state ultraviolet laser dicing of silicon carbide chips using design of experiment methodology, J. Laser Appl. 27 (2015) 32009. doi:10.2351/1.4919886.

[22] A. Ben-Yakar, R.L. Byer, Femtosecond laser ablation properties of borosilicate glass, J. Appl. Phys. 96 (2004) 5316. doi:10.1063/1.1787145.

Supplementary Data

Table 1S: Experimental factors, responses and S/N ratio of the Taguchi matrix L_{16} (4^5) used for the ZF14 – 188 µm ZeonorFilm®

Sample	Fluence (J/cm^2)	Scan Speed (mm/s)	Number of Passes	Depth (µm)	FWHM (µm)	Signal/Noise Depth (dB)	Signal/Noise FWHM (dB)
1	0.652	1.8	1	6.06	30.60	15	-29
2	0.652	2.5	2	4.09	30.77	12	-29
3	0.652	3	3	4.13	30.12	12	-29
4	0.652	3.5	4	2.98	32.14	9	-30
5	0.785	1.8	2	13.31	50.46	22	-34
6	0.785	2.5	1	8.99	42.85	19	-32
7	0.785	3	4	14.02	60.51	22	-35
8	0.785	3.5	3	14.09	60.47	22	-35
9	0.896	1.8	3	54.63	61.28	34	-35
10	0.896	2.5	4	28.33	74.46	29	-37
11	0.896	3	1	22.21	67.08	26	-36
12	0.896	3.5	2	25.07	76.58	27	-37
13	0.983	1.8	4	86.94	56.32	38	-35
14	0.983	2.5	3	42.01	57.85	32	-35
15	0.983	3	2	16.77	55.95	24	-34
16	0.983	3.5	1	15.15	62.53	23	-35

345
346 Table 2S: Experimental factors. responses and S/N ratio of the Taguchi matrix L32 ($21 + 4^9$) used for the ZF-16 ZeonorFilm®

Sample	Thickness (μm)	Fluence (J/cm^2)	Scan Speed (mm/s)	Number of Passes	Depth (μm)	FWHM (μm)	Signal/Noise Depth (dB)	Signal/Noise FWHM (dB)
1	100	0.652	1.8	1	14.15	26.21	23.0160	-28.3696
2	100	0.652	2.5	2	10.34	24.47	20.2902	-27.7727
3	100	0.652	3	3	7.32	24.63	17.2885	-27.8277
4	100	0.652	3.5	4	8.36	25.03	18.4404	-27.9708
5	100	0.785	1.8	2	18.61	27.67	25.3929	-28.8406
6	100	0.785	2.5	1	13.11	26.15	22.3490	-28.3485
7	100	0.785	3	4	29.13	48.95	29.2871	-33.7959
8	100	0.785	3.5	3	28.62	38.56	29.1338	-31.7226
9	100	0.896	1.8	3	48.50	91.58	33.7149	-39.2358
10	100	0.896	2.5	4	42.97	62.65	32.6627	-35.9382
11	100	0.896	3	1	44.77	68.81	33.0197	-36.7528
12	100	0.896	3.5	2	59.64	75.36	35.5107	-37.5428
13	100	0.983	1.8	4	45.50	76.54	33.1608	-37.6776
14	100	0.983	2.5	3	42.74	85.12	32.6171	-38.6010
15	100	0.983	3	2	33.26	70.35	30.4375	-36.9450
16	100	0.983	3.5	1	49.91	106.24	33.9640	-40.5260
17	250	0.652	1.8	1	5.65	28.28	15.0459	-29.0286
18	250	0.652	2.5	2	5.86	28.18	15.3569	-28.9986
19	250	0.652	3	3	3.64	27.63	11.2208	-28.8272
20	250	0.652	3.5	4	2.56	31.13	8.1499	-29.8635
21	250	0.785	1.8	2	5.36	33.25	14.5752	-30.4361
22	250	0.785	2.5	1	6.51	27.95	16.2752	-28.9278
23	250	0.785	3	4	9.54	45.68	19.5947	-33.1943
24	250	0.785	3.5	3	6.36	35.05	16.0720	-30.8948
25	250	0.896	1.8	3	37.98	74.35	31.5913	-37.4254
26	250	0.896	2.5	4	9.95	54.53	19.9524	-34.7324
27	250	0.896	3	1	11.61	33.28	21.2933	-30.4435
28	250	0.896	3.5	2	13.56	44.43	22.6464	-32.9532
29	250	0.983	1.8	4	83.43	54.69	38.4265	-34.7582
30	250	0.983	2.5	3	57.36	68.16	35.1723	-36.6703
31	250	0.983	3	2	38.55	97.86	31.7213	-39.8123
32	250	0.983	3.5	1	33.86	63.46	30.5925	-36.0503

347

348 Table 3S: ANOVA of the depth response for the design of the ZF14–188 ZeonorFilm®.

Source	Sum of Squares	df	Mean Square	F Value	p-value (Prob > F)
Model	0.275614	4	0.068903	67.3542	< 0.0001
F	0.02454	1	0.02454	23.98814	0.0005
N	0.025638	1	0.025638	25.06201	0.0004
FN	0.024814	1	0.024814	24.25653	0.0005
F^2	0.028973	1	0.028973	28.32147	0.0002
Residual	0.011253	11	0.001023		
Cor Total	0.286867	15			
R^2	0.960773			Pred R-Squared	0.911214
Adj R-Squared	0.946508			Adeq Precision	25.12639

349

Table 4S: ANOVA of the FWHM response for the design of the ZF14–188 ZeonorFilm®.

Source	Sum of Squares	df	Mean Square	F Value	p-value (Prob > F)	
Model	3330.642	5	666.1285	25.3565	< 0.0001	significant
F	744.6646	1	744.6646	28.34601	0.0003	
ν	159.0075	1	159.0075	6.052696	0.0337	
N	181.5339	1	181.5339	6.910175	0.0252	
Fν	146.2114	1	146.2114	5.565608	0.0400	
F^2	810.5034	1	810.5034	30.85219	0.0002	
Residual	262.7053	10	26.27053			
Cor Total	3593.348	15				
R-Squared	0.926891			Pred R-Squared	0.816209	
Adj R-Squared	0.890337			Adeq Precision	13.41669	

Table 5S: ANOVA of the depth response for the design of the ZF16–100 and ZF16-250 ZeonorFilm®.

Source	Sum of Squares	df	Mean Square	F Value	p-value (Prob > F)	
Model	24.38372	7	3.483389	22.24774	< 0.0001	significant
d	0.500087	1	0.500087	3.193963	0.0865	
F	18.24503	1	18.24503	116.5275	< 0.0001	
ν	0.000985	1	0.000985	0.006291	0.9374	
N	0.187634	1	0.187634	1.198384	0.2845	
dF	0.719099	1	0.719099	4.592748	0.0425	
dν	0.472094	1	0.472094	3.015172	0.0953	
FN	0.17981	1	0.17981	1.148414	0.2945	
Residual	3.757745	24	0.156573			
Cor Total	28.14147	31				
R-Squared	0.866469			Pred R-Squared	0.770109	
Adj R-Squared	0.827523			Adeq Precision	16.3143	

Table 6S: ANOVA of the FWHM response for the design of the ZF16–100 and ZF16-250 ZeonorFilm®.

Source	Sum of Squares	df	Mean Square	F Value	p-value (Prob > F)	
Model	0.033694	6	0.005616	27.22462	< 0.0001	significant
d	0.001231	1	0.001231	5.96651	0.0220	
F	0.019155	1	0.019155	92.86301	< 0.0001	
ν	0.001084	1	0.001084	5.257444	0.0305	
dF	0.001157	1	0.001157	5.607571	0.0259	
Fν	0.001065	1	0.001065	5.165116	0.0319	
FN	0.001961	1	0.001961	9.504866	0.0049	
Residual	0.005157	25	0.000206			
Cor Total	0.038851	31				
R-Squared	0.867267			Pred R-Squared	0.798998	
Adj R-Squared	0.835411			Adeq Precision	15.13616	

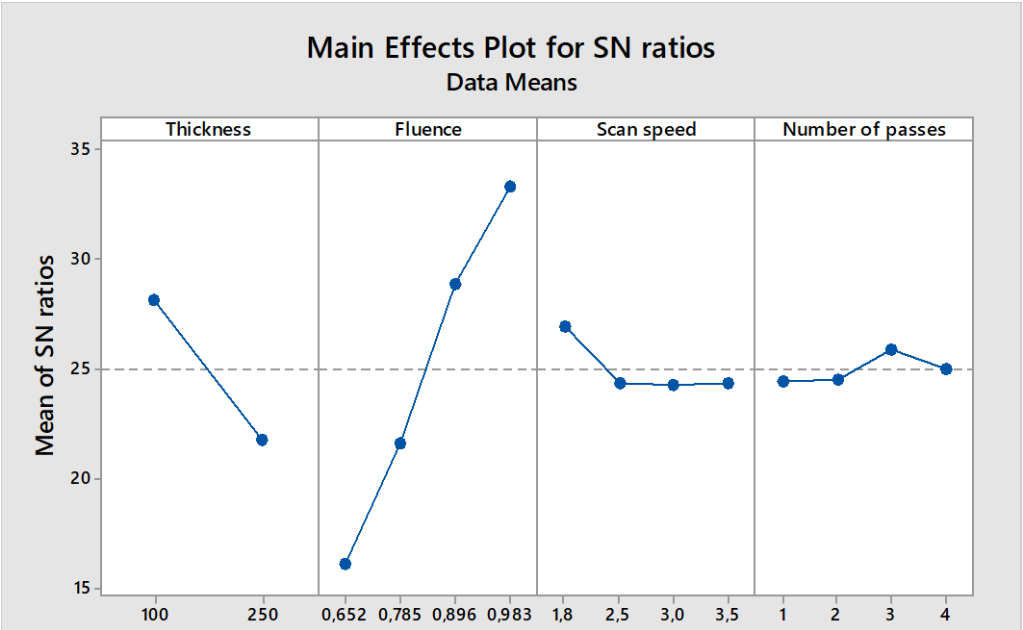

357

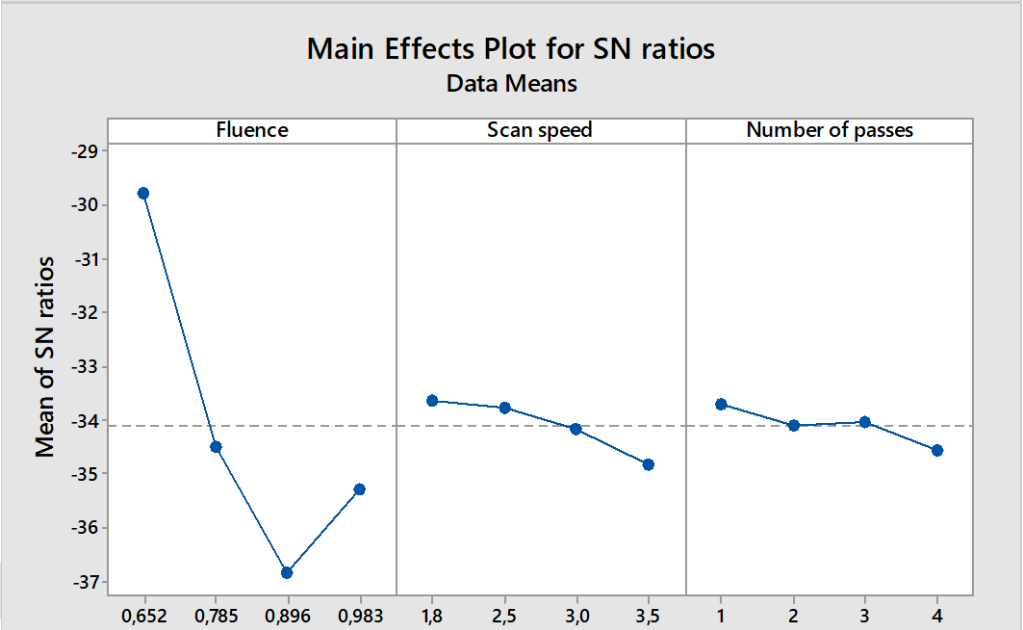

358
359 Figure 1S: Effects plot for the S/N ratio of (a) depth and (b) FWHM of the ZF14.
360

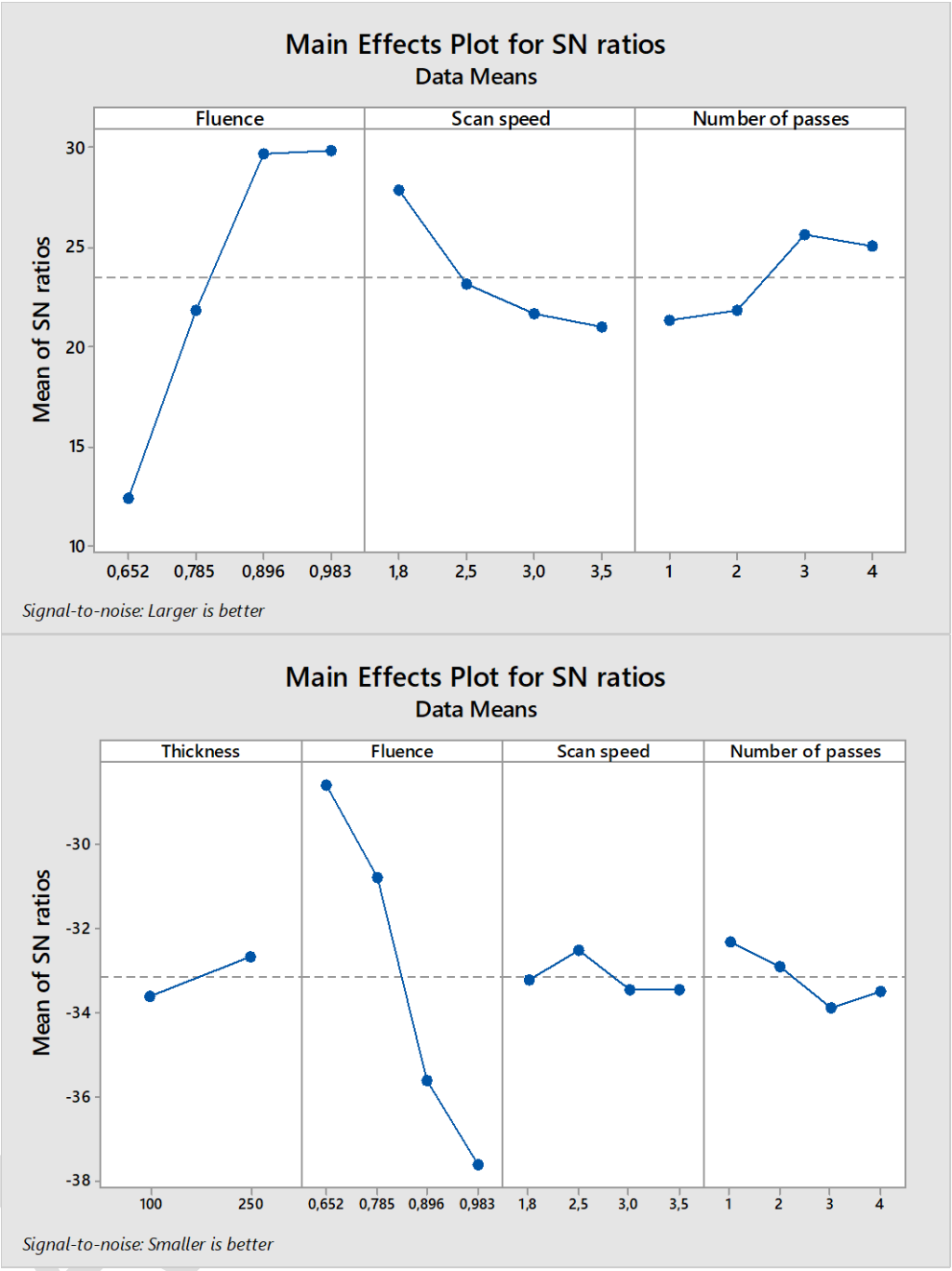

Figure 2S: Effects plot for the S/N ratio of (a) depth and (b) FWHM of the ZF16.